



# Numerical study of dust plume impact on urban thermal comfort

Jérémy Bernard<sup>1,2</sup>, Tim Nagel<sup>1</sup>, Valéry Masson<sup>1</sup>, Aude Lemonsu<sup>1</sup>, Jean Wurtz<sup>1</sup>, Pierre Tulet<sup>3</sup>, and Ouentin Rodier<sup>1</sup>

<sup>1</sup>Météo-France, CNRS, Univ. Toulouse, CNRM, Toulouse, France

**Correspondence:** Jérémy Bernard (jeremy.bernard@zaclys.net)

Abstract. In Europe, heatwave conditions associated with southern synoptic flows can sometimes be combined with dust plume events coming from the Saharian desert. The aerosol plume modifies the radiation observed near the ground and consequently other variables such as air temperature. This study focuses on a heatwave and its corresponding plume of Saharian dusts that have reached the Paris region from 15 to 19 June 2022. To investigate the aerosols impact on the thermal comfort, three numerical simulations based on the Meso-NH model are used: one without dust aerosol (C0), one with CAMS dust data (C1) and one with twice the concentration of CAMS dust data (C2). Simulation C1 is validated against observations from the PANAME-Urban experimental campaign. The impact of aerosols on Aerosol Optical Depth and incoming solar radiation at the surface are well reproduced, and the air temperature and boundary layer heights are improved when taking into consideration the aerosols. The presence of a dust plume during the heat wave contributes to reduce solar radiation and air temperature to up to 75 W/m² and 1 K, respectively. At 16:00 UTC in sunny places of urban and suburban areas, it results in a thermal comfort improvement of up to 1°C. However, in the shade of suburban areas, the increase of diffuse radiation and relative air humidity as well as the decrease of wind speed induced by the dust aerosols counterbalance the air temperature decrease, thus leading to no improvement of the thermal comfort.

# 1 Introduction

Atmospheric aerosols, including mineral dust, play a critical role in modulating weather and climate. As reviewed by Schepanski (2018) and references therein, dust particles are formed through natural processes and can be transported from one continent to an other, influencing atmospheric chemistry, radiation, and cloud microphysics. Their impacts are particularly relevant during large-scale dust outbreaks, which strongly modify surface and boundary layer conditions.

One of the mechanisms by which aerosols affect the atmosphere is through their interaction with radiation. Depending on their optical and microphysical properties, aerosols can scatter and absorb solar shortwave (SW) and longwave (LW) radiation, thereby altering the surface and atmospheric energy budget. The use of an aerosol climatology for global models based on the tropospheric aerosol scheme shows an effect of up to  $30 \ W/m^2$  over desert, partly compensated by the increase of LW radiations (about  $10 \ W/m^2$  - Wang et al. (2022)). Observational studies of a Saharan dust outbreak over Barcelona confirm this level of magnitude: in June, Córdoba-Jabonero et al. (2021) documented that when the aerosol optical depth (AOD) reached

<sup>&</sup>lt;sup>2</sup>EDYTEM, CNRS, Le Bourget du Lac, France

<sup>&</sup>lt;sup>3</sup>LAERO, Laboratoire d'Aérologie (UMR 5560 CNRS, UT3, IRD), Toulouse, France





0.45 at 532 nm, the decrease in net SW radiation was  $54 W/m^2$  while the increase in net LW radiation was  $11 W/m^2$ . Similarly, at the end of May, Bangert et al. (2012) reported that including dust–radiation interactions in a simulation of a Saharan dust event in southwest Germany reduced the net SW radiation by up to  $80 W/m^2$  (for an AOD of 0.36).

These radiative perturbations directly affect the near-surface air temperature. Bangert et al. (2012) simulation reduced significantly (up to 1 K) the positive bias in the forecast of near-surface air temperature. During the 2003 European heatwave, characterized by AOD values between 0.4 and 0.6, numerical experiments with the Weather Research and Forecasting Model (WRF, Skamarock et al., 2005) indicated that aerosols reduced net SW radiation by  $30–50~W/m^2$ , corresponding to a 15% reduction in solar flux (Péré et al., 2011). This decrease in surface energy led to air temperature reductions of up to 0.3 K, consistent with other observational estimates (Zhang et al., 2010). Closer to the dust emission source, the impacts of dust aerosols can be more important: for a dust storm in West Africa, where the dust was located over the boundary layer, the reduction in the near-surface temperature reached 4 K (Tulet et al., 2008).

Wang et al. (2022) emphasizes that the vertical distribution of absorbing aerosols is crucial: heating near the surface can enhance entrainment in the planetary boundary layer (PBL), whereas heating aloft tends to stabilize the atmosphere by strengthening the inversion layer. Thus, through their effect on radiation and surface temperature, aerosols also exert strong control on turbulence, PBL dynamics, and wind fields. Reduced surface heating weakens turbulent mixing, leading to a shallower boundary layer and lower wind speeds. For example, Péré et al. (2011) reported reductions in PBL height of 200 m (10%) and wind speed decreases of 1.2 m/s (6%) in response to aerosol–radiation interactions. Observations by Park et al. (2010) further support this, showing wind speed reductions up to 20% when surface solar flux was suppressed by  $200 \ W/m^2$  due to Asian dust layers.

Anthropogenic aerosols are among the largest sources of uncertainty in radiative forcing (Stocker et al., 2013). Mitigation policies have already demonstrated a reduction of the aerosols concentration (Hodnebrog et al., 2024). Thus the trend being at adding more stringent mitigation policies to improve air quality, aerosol emissions are likely to be reduced worldwide during the 21st century. Zhao et al. (2019) have investigated the effect of the projected aerosol decrease on the worldwide increase of intensity, frequency, and duration of heat waves. Their results show that future green house gases increase will result in future (2081–2100) heatwaves that are, when globally averaged over land, significantly more intense (+2.4 K on average air temperature), longer (17 days) and more frequent (12 more per year), compared to present-day. These changes will also be further aggravated by aerosol reductions, leading to an increase of their mean intensity, length and frequency by 0.6 K, 7 days, and 2 more per year, respectively.

Although there is a quite dense literature showing the impact of aerosols on near-surface atmospheric variables, most of them are performed at coarse resolution (12 km to 36 km - Bernstein et al. (2013) and Péré et al. (2011), respectively) and, to the best of the authors knowledge, none are dedicated to evaluate the impact on human thermal comfort. More specifically, urban areas, where most of the population is concentrated, are already impacted by their local climate (Oke et al., 2017) and might be directly affected by the presence of large amounts of aerosols in the atmosphere. Indeed, the shadow provided by buildings can be seen as cool places during clear days (Masson et al., 2020) but these areas might be affected by the interactions between aerosols and radiation in the atmosphere. To study how the aerosol concentration can impact thermal comfort in urban





areas, we simulate a heatwave event in the Paris region associated with an inter-continental Saharan dust outbreak using an atmospheric model coupled with an urban surface model at a resolution of 1.2 km.

#### 2 Material and method

# 2.1 Meteorological overview

The present study focuses on the heatwave period that strokes the Paris region from 15 to 19 June 2022. The synoptic overview of this event, based on the ERA5 reanalysis (Hersbach et al., 2023), is presented in Fig. 1. The temperature at 850 hPa in the Paris region gradually warms up to 20°C from 15 to 18 June under the influence of a 500 hPa cut-off located west of Portugal that generates advection of hot air from North Africa and the Iberian Peninsula toward France. In addition, a high geopotential at 500 hPa grows over France leading to air subsidence further increasing the near-surface air temperature. The 850 hPa temperature warms until 18 June, which was classified as a notable heat peak day by Météo-France and the Public Health Agency (Lemonsu et al., under rev.). This episode ended on the night from 18 to 19 June, as the low-pressure system moved northeastward, bringing cooler oceanic air over France and leading to important rainfall and temperature drop over the Paris region.

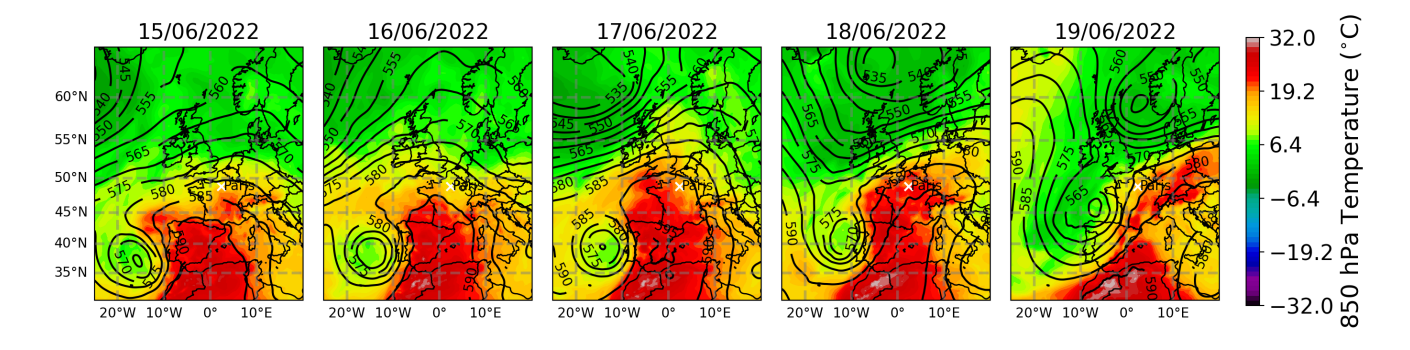


**Figure 1.** Synoptic overview at 12:00 UTC from 15 to 19 June 2022 based on ERA5 reanalysis (Hersbach et al., 2023). The colours and the contours represent the temperature at 850 hPa and the 500 hPa geopotential height.

This heat episode was not only remarkable because it was the earliest ever recorded heatwave in France, but also because a Saharan dust event outbreak occurred simultaneously, driven by the strong southerly flow. The dust AOD at 550 nm, based on the CAMS reanalysis (Rémy et al., 2022), is mapped from 15 to 19 June 2022 in Fig. 2. The dust plume reaches the Paris region in the afternoon of 16 June and begins to leave it on 19 June as the low-pressure system moves northeastward. Note that observations derived from ground ceilometers in the Paris region show that before 17 June the aerosols were in the troposphere, so interactions with aerosols in the boundary layer was not possible before this date.





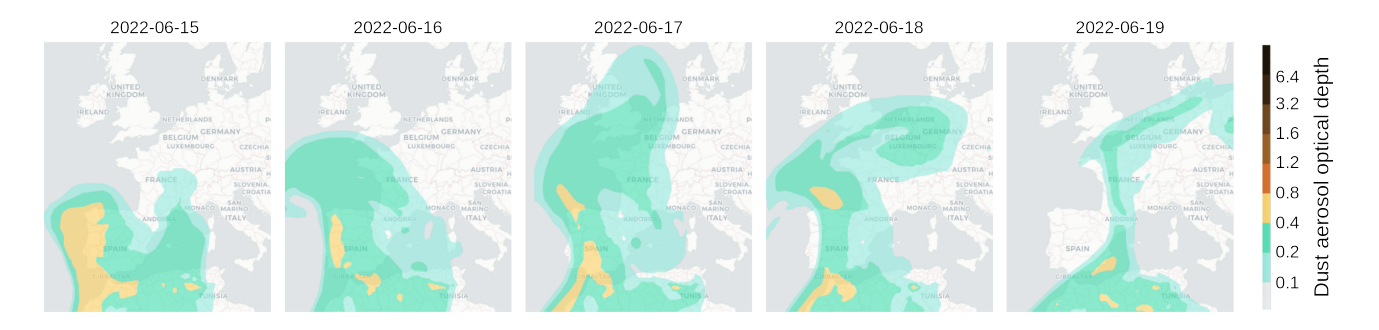


**Figure 2.** Dust aerosol optical depth (550 nm) every day at noon from 15 to 19 June 2022 based on CAMS reanalysis (Rémy et al., 2022). Source: Dust data and/or images were provided by the WMO Barcelona Dust Regional Center and the partners of the Sand and Dust Storm Warning Advisory and Assessment System (SDS-WAS) for Northern Africa, the Middle East and Europe.

The CAMS data, used as input for this study, are compared with other dust data sources at the Palaiseau station location (~20 km southwest of Paris) in Fig. 3. The models have been chosen to highlight the variability of the AOD values: SILAM (Sofiev et al., 2015) has the minimum AOD values, ZAMG-WRF-CHEM (LeGrand et al., 2019) the maximum, while MULTI-MODEL, a multi-model ensemble (Basart et al., 2019) can be seen as median values. For this period, the CAMS-IFS (Rémy et al., 2022) is quite close to the MULTI-MODEL. The observations have an offset of about 0.1 which is particularly visible on the first two days. This offset is due to the model AOD definition, limited to dust particles, while the observations are affected by all types of aerosols. From the end of 16 June and until 19 June, the temporal variability is well represented by all the models: there is an increase of the AOD during the 16 to 17 night, a slight decrease during 17 June and the highest values during the next night and day. Only the SILAM data does not have clear higher AOD values on 18 June. However, there is a large variability in terms of AOD intensity, the dust AOD on 18 June ranging between 0.1 in SILAM and up to 0.5 in ZAMG-WRF-CHEM. The variability of the AOD values between the data source can be part ly attributed to their quite large spatial resolution, from 0.2° for ZAMG-WRF-CHEM and SILAM, to 0.75° for CAMS.



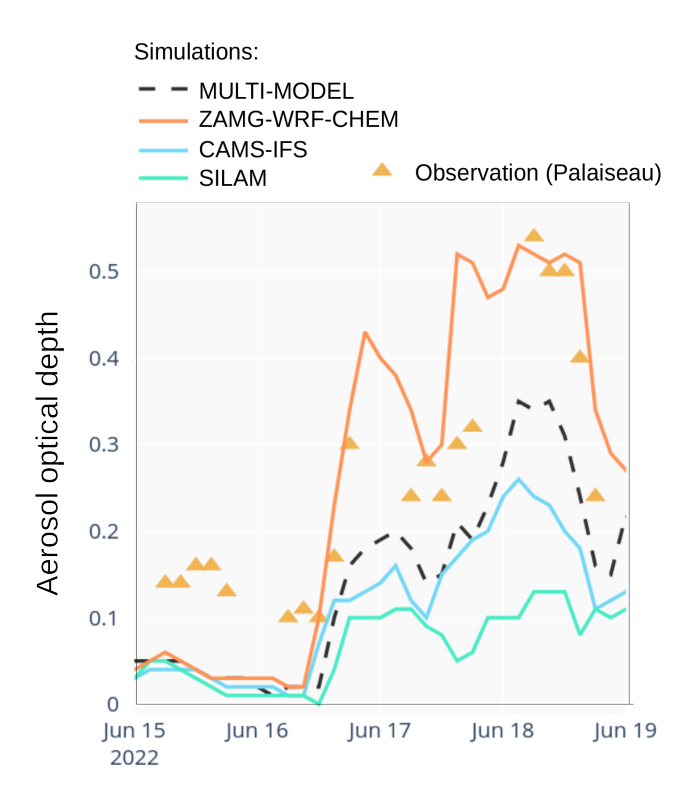


**Figure 3.** Aerosol optical depth at 550 nm from 15 to 19 June 2022. The observation is the total aerosol optical depth at the Palaiseau station while the model data is only the effect of the dust aerosols. The choice of the models was performed in order to illustrate the variability of the dust AOD values: ZAMG-WRF-CHEM, CAMS-IFS, SILAM and MULTI-MODEL. Dust data and/or images were adapted from the WMO Barcelona Dust Regional Center and the partners of the Sand and Dust Storm Warning Advisory and Assessment System (SDS-WAS) for Northern Africa, the Middle East and Europe.

## 2.2 Model and Numerical experiments

100

In this study, the non-hydrostatic research atmospheric model Meso-NH (Lac et al., 2018) is coupled with the SURFace Externalised Land Surface Model (SURFEX, Masson et al., 2013) over a single 480 km by 480 km domain of 1.2 km horizontal resolution, covering the northern part of France and centered on Paris (Fig. 4). For the wind advection, a third-order weight essentially non-oscillatory scheme (WENO3) is used and combined with a five-stage third-order Runge-Kutta time-splitting scheme (Lunet et al., 2017). The model time step is set at 5 seconds. The atmospheric turbulence scheme, based on a prognostic equation for the turbulent kinetic energy (Cuxart et al., 2000), only accounts for vertical turbulent fluxes and is closed with the mixing length of Honnert et al. (2021). Deep convection is explicitly resolved while shallow convection is parameterized with an Eddy-Diffusivity-Kain-Fritsch scheme (Pergaud et al., 2009). The historical radiative solver of Meso-NH is used: the Rapid Radiation Transfer Model (Mlawer et al., 1997) for LW radiation is coupled with a SW scheme based on the Fouquart (1980) method. Finally, microphysics is solved using the ICE3 one-moment scheme (Pinty and Jabouille, 1998;



105

110

120

125

135



Riette, 2020; Wurtz et al., 2023).

Surface physics is handled by the last version of SURFEX (V9.0), and the component fraction of the four tiles per grid cell is given by the ECOCLIMAP-SG land cover database (Wiki – CNRM, 2018). Each tile uses a dedicated scheme to calculate the fluxes over the surface. For urban tiles, the multilayer version of the TEB urban canopy model (Masson, 2000; Schoetter et al., 2020) is used, allowing the buildings to interact directly with the first atmospheric layers using a drag approach and releasing fluxes at the corresponding atmospheric model levels. In-canyon urban vegetation and street trees are also taken into account (Redon et al., 2017, 2020). For rural and natural tiles, the Soil-Biosphere-Atmosphere interaction land surface model (Noilhan and Planton, 1989, ISBA) is used, with an explicit multi-layer soil approach (Decharme et al., 2011). The ISBA Multi-Energy Budget parameterization (Boone et al., 2017, MEB) is used, allowing to model a low and high vegetation canopy that is separated from the ground.

Currently, Meso-NH is coupled with the explicit CAMS aerosol data. However, due to the large variability of AOD values obtained in the various models used to predict dusts (Fig. 3), three simulations are performed: i) C0 uses the dust concentration set to 0, ii) C1 uses the CAMS data as input, and iii) C2 uses twice the CAMS data values as input.

Except for dust data, the numerical configuration for these three simulations is identical and adapted from other studies of the PANAME-Urban framework (Forster et al., 2024; Lemonsu et al., under rev.). The vertical grid is divided in 68 levels with a first half-level at 2 m for physical variables such as temperature. The grid size increases along the vertical, with a constant stretching of 1.17 up to 1000 m and 1.04 above. The domain extends vertically up to approximately 17,500 m. The maximum vertical grid size allowed is 500 m.

The amount of dust aerosols is set according to the CAMS global reanalysis (Inness et al., 2019). It is provided as a concentration in  $\mu g/m^3$  for each cell of 0.75° by 0.75° (80 km by 80 km) with 35 vertical layers within the model domain extension. The inclusion of CAMS aerosols into the Meso-NH model is prone to uncertainties. The total mass content given by CAMS is distributed according to log-normal modes that can be described by the 0th, 3rd, and 6th moment of the distribution (Grini et al., 2006; Hoarau et al., 2018). Assumptions are made on the shape of the distributions of aerosols, which influence the radiative properties. Note that for simplification, only dust transport is included in the simulations. Due to the short period of simulation and the fact that the aerosols are outside of the boundary layer, the modification of the aerosols content by deposition, aggregation or chemical reaction is not simulated. For all non-desertic types of aerosols, in each simulation, the Tegen et al. (1997) six-class aerosol climatology is used.

Each simulation (C0, C1 and C2) consists of a single 4-days Meso-NH run. The initial conditions for the atmospheric and surface fields, as well as the atmospheric boundary conditions, come from the AROME-France analysis (Seity et al., 2011; Brousseau et al., 2016), which includes data assimilation and is also coupled with SURFEX.

#### 2.3 Observation network

The simulations presented above can be compared with numerous meteorological observations, distributed over the Ile-de-France administrative region (which includes Paris). The measurement types and their location are shown in Fig. 4 and described hereafter.





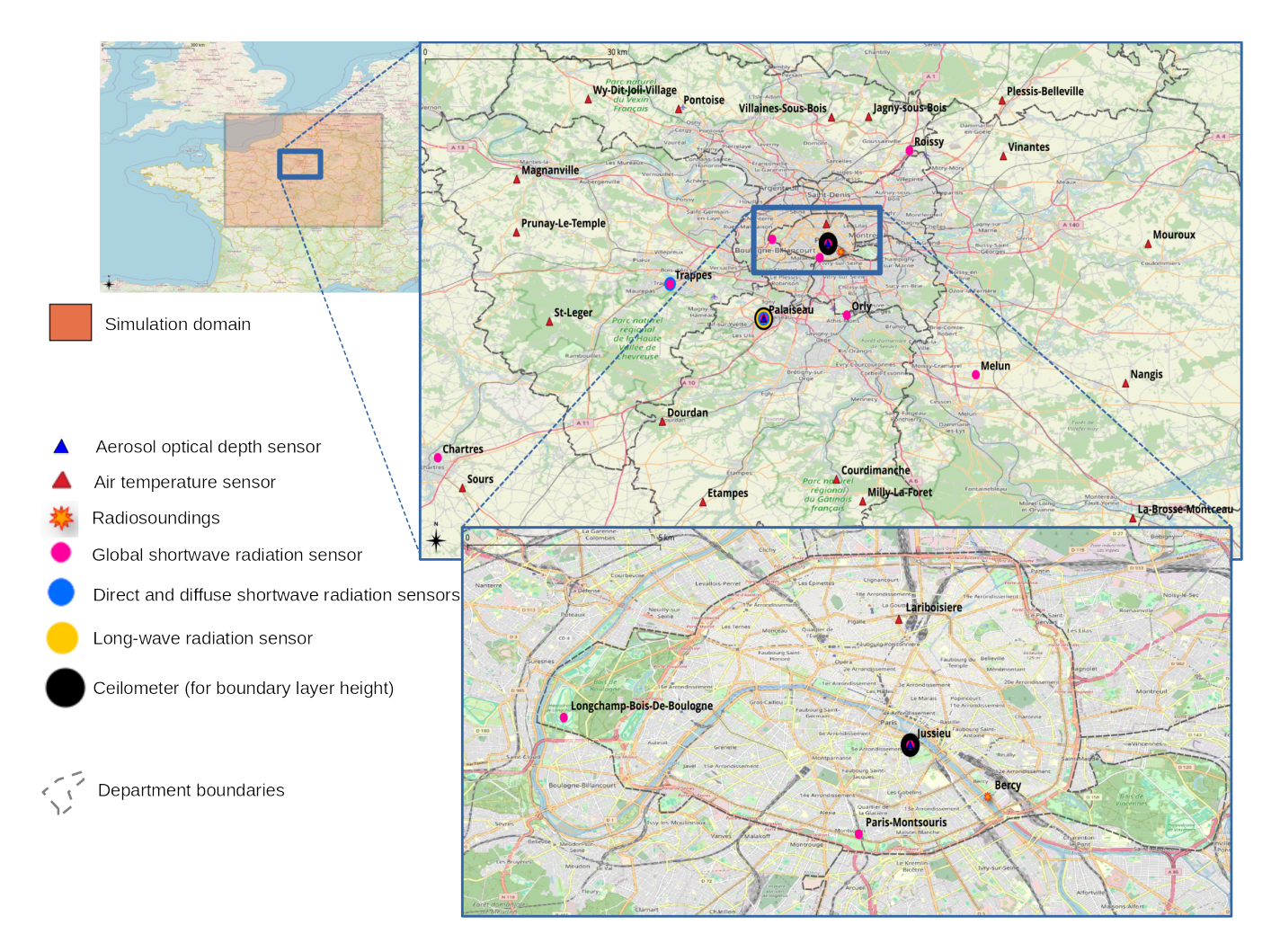


**Figure 4.** Representation of the model configuration and observation network. ©OpenStreetMap contributors 2025. Distributed under the Open Data Commons Open Database License (ODbL) v1.0.

The AOD, for wavelengths included between 340 and 1640 nm, is observed by two AERONET stations (Holben et al., 1998): one is located in the center of Paris and the second is at Palaiseau.

The Météo-France permanent surface network (RADOME, Tardieu and Leroy, 2003) has nine automatic weather stations (AWS) located nearby Paris that have global SW radiation sensors. Two of them also record direct and diffuse SW radiation (Trappes and Palaiseau) and one record the LW radiation (Palaiseau).

Comparing atmospheric model simulations with observations of 2 m air temperature in cities is not straightforward, due to the lack of representativeness of AWS stations (Oke et al., 2004). Indeed, to follow the recommendations of the World Meteorological Organization, AWS operated by national meteorological services should be installed in large and homogeneous areas of flat terrain and low-rise vegetation. Finding sites that match these constraints is particularly complex in or near urban areas, which are characterized by a quite high land cover heterogeneity and thus far from the standard large area of grass





vegetation. Thus, in suburban areas, the stations are often located in small patches of low-rise vegetation areas in airports, and in cities, they are often located in urban parks. Because, in the present study, the model grid mesh is 1.2 km, a single cell often includes both urban and rural land cover types. This is particularly remarkable in or nearby large urban areas. Although the observation station is located in a low-rise vegetation area of 200-500 m wide, the grid cell will simulate fluxes released by the low-rise vegetation area but also by a large amount of urbanized surfaces, making the comparison impossible. To prevent this inconsistency, only a sample of all the RADOME stations located in the study area is chosen: 17 stations defined as 'rural' and a unique station defined as 'urban' (Lariboisière) are selected. All 'rural' stations have less than 20% of their surface covered by urban features (the urban fraction is calculated as a bilinear interpolation of the urban fraction of the four closest grid cells) while the 'urban' site is located in a non-vegetated part of Paris city center and the model cell where it is located being 100% urban.

The air temperature of the upper atmosphere is observed using radiosondes measurements released from the inner part of Paris (location called Radiosoundings in Fig. 4). The atmospheric boundary layer height is also estimated from two ceilometers, located in Jussieu and Palaiseau, using the algorithm described by Kotthaus et al. (2020). Note that more details on each instrument can be found in the description of the PANAME-Urban experimental campaign (Lemonsu et al., under rev.).

# 160 3 Results

155

The simulations without dust (C0) and with CAMS dust aerosols (C1 and C2) are compared with the observations on the Paris region to assess the quality of the simulations, as well as the impact of aerosols on radiation and air temperature. Then, the effect of aerosols on the thermal comfort during the heatwave is investigated in Sec. 3.4. In the following sections, if not specified, the simulated data refers to the simulation C1.

# 165 3.1 Aerosol optical depth

According to Fig. 5, the AOD simulated by C1 and observed in the Paris region agree well. For both observations and simulations, the aerosols start to affect the AOD on the afternoon of 16 June, the maximum AOD being on 18 June while 15 June is the day with the lowest AOD mean. Figures 5a-c show that the higher the wavelength, the lower the AOD but also that for all wavelengths, the increase of AOD between 15 and 18 June is nearly the same (about 0.3). Last, the AOD difference between the location of the two nearby AOD stations (Paris and Palaiseau are located about 20 km apart - Fig. 4) is low (< 0.07 for observations and < 0.05 for simulations).

However, differences are also observed. First, there is a small negative bias (about 0.1) of the simulated AOD. This bias is not constant over time, even when there is no dust plume, *i.e.*, on 15 June. This may be due to the use of a climatological value for all non-desertic aerosols with the Tegen et al. (1997) climatology, whose values are expected to be representative of a monthly mean, and may underestimate their concentration during clear sky heatwave conditions. Concerning the dust plume, the AOD increase (on 16 June) and decrease (on 18 June) is much sharper in the observation than in the simulation, which is probably explained by the low resolution of the initial field provided by the CAMS data. Also, and contrary to the three other





days, the observed AOD on 17 June is lower than the simulated one. For this reason, the effects of the aerosols on the surface variables are expected to be more accurately simulated on 18 June (especially morning) than on 17 June.

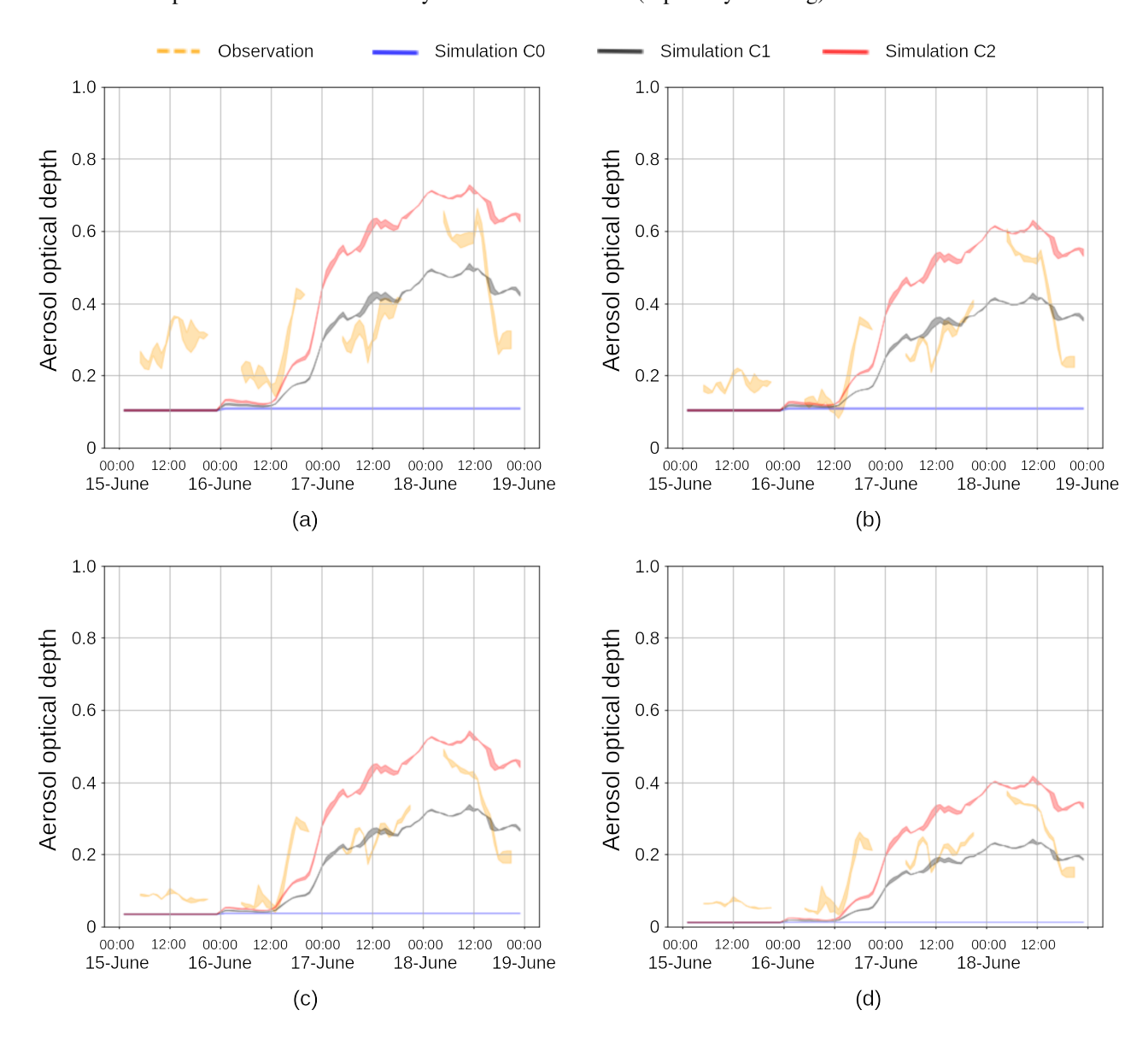


Figure 5. The aerosol optical depth observed (and simulated) at the Palaiseau station (a) at 340 nm (250-440 nm), (b) at 500 nm (440-690 nm), at 1020 nm (690-1190 nm) and (d) at 1640 nm (1190, 2380 nm).

## 180 3.2 Radiation

The 4-days heatwave event investigated includes a day without dust plume but with a partially cloudy sky (15 June), followed by 3 days with increasing dust aerosols above the Paris region. These conditions affect the global downward solar radiation: on



185

190

195



15 June, the observed and simulated data show a signal shape and maximum intensity altered by the clouds, both in Chartres (Fig. 6a) and in Roissy (Fig. 6b). On 16 June, the aerosol cloud reaches the Paris region from the South-West, affecting the Western part of the region (Fig. 6a) more than the Eastern one (Fig. 6b).

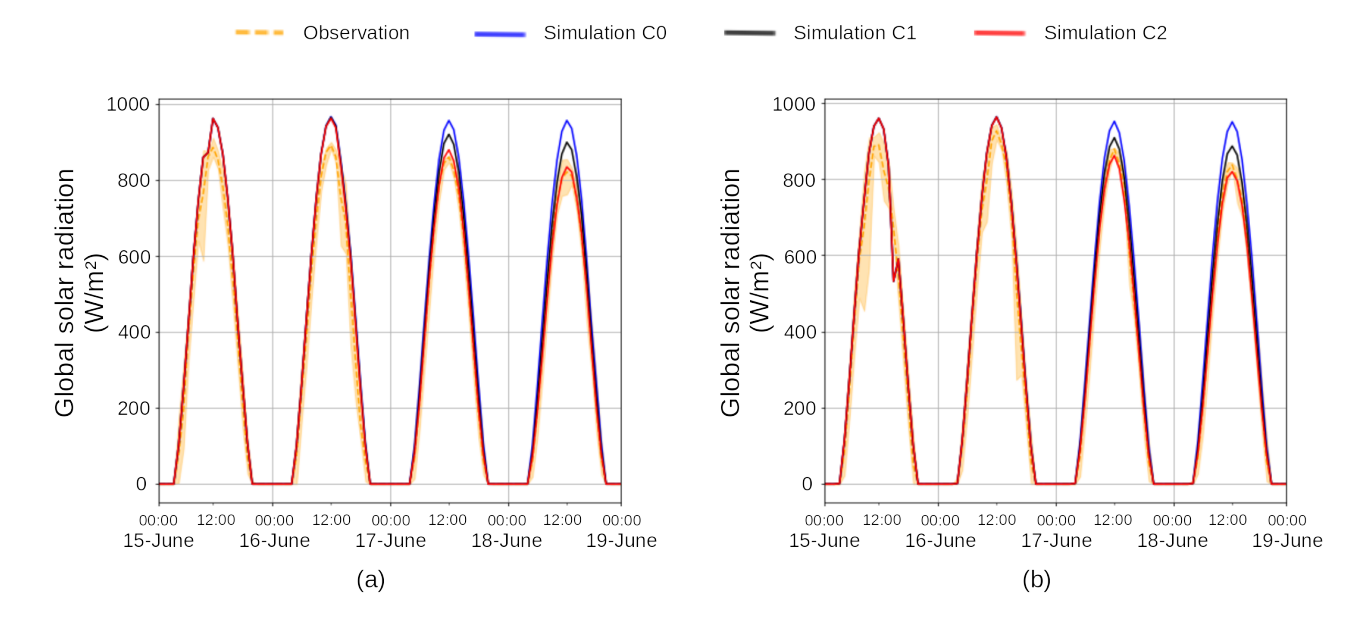


**Figure 6.** The global downward solar radiation (a) in Chartres, the most Western radiation station, and (b) in Roissy, the most Eastern radiation station. Note that the observation line is the hourly average value and is surrounded by a patch delineated at the bottom and at the top by the hourly minimum and maximum, respectively.

For the first two days, where there is a limited amount of aerosols in the atmosphere, the simulation overestimates the observed radiation. This could be caused by the presence of contrails and sparse cumulus humilis on the 15 June morning and afternoon respectively (not shown), that are not simulated by the model. The underestimation of the non-desertic AOD (Sect. 3.1) could also contribute to this bias. However, while there is a general negative offset of the simulated AOD, the AOD increase between 15 and 18 June is nearly the same for simulations and observations (see Sect. 3.1). Therefore, to evaluate the ability of the model to simulate the effect of the increase of dust aerosols on global radiation, the global radiation from 15 June is subtracted that of 17 and 18 June (Fig. 7a). The nine in situ AWS equipped to measure radiations are used to produce this figure in order to illustrate the spatial variability of the effects. On 17 June, the C1 simulation overestimates the effect of the aerosols, which is consistent with the AOD overestimation shown in Sect. 3.1. On 18 June, the C1 simulation performs well in the morning with an effect of up to 75 W/m² in the simulation versus 65 W/m² in the observations. However, during the afternoon, the effect of the aerosols on the global solar radiation is again highly overestimated (about 30 W/m² offset). Again, this is understandable looking at the AOD (Fig. 5): in the afternoon, the observed AOD drops very quickly while it decreases very slowly in the simulations, leading to a large overestimation of the simulated AOD. Note that the spike in the simulations occurring in the afternoon is due to the presence of clouds in the Eastern part of the region during the reference day (15 June -





Fig. 6b). Overall, on 18 June, the daily mean effect of the aerosol on global radiation has the same order of magnitude between the simulation C1 (-32  $W/m^2$ ) and the observations (25  $W/m^2$  - Tab. 1).

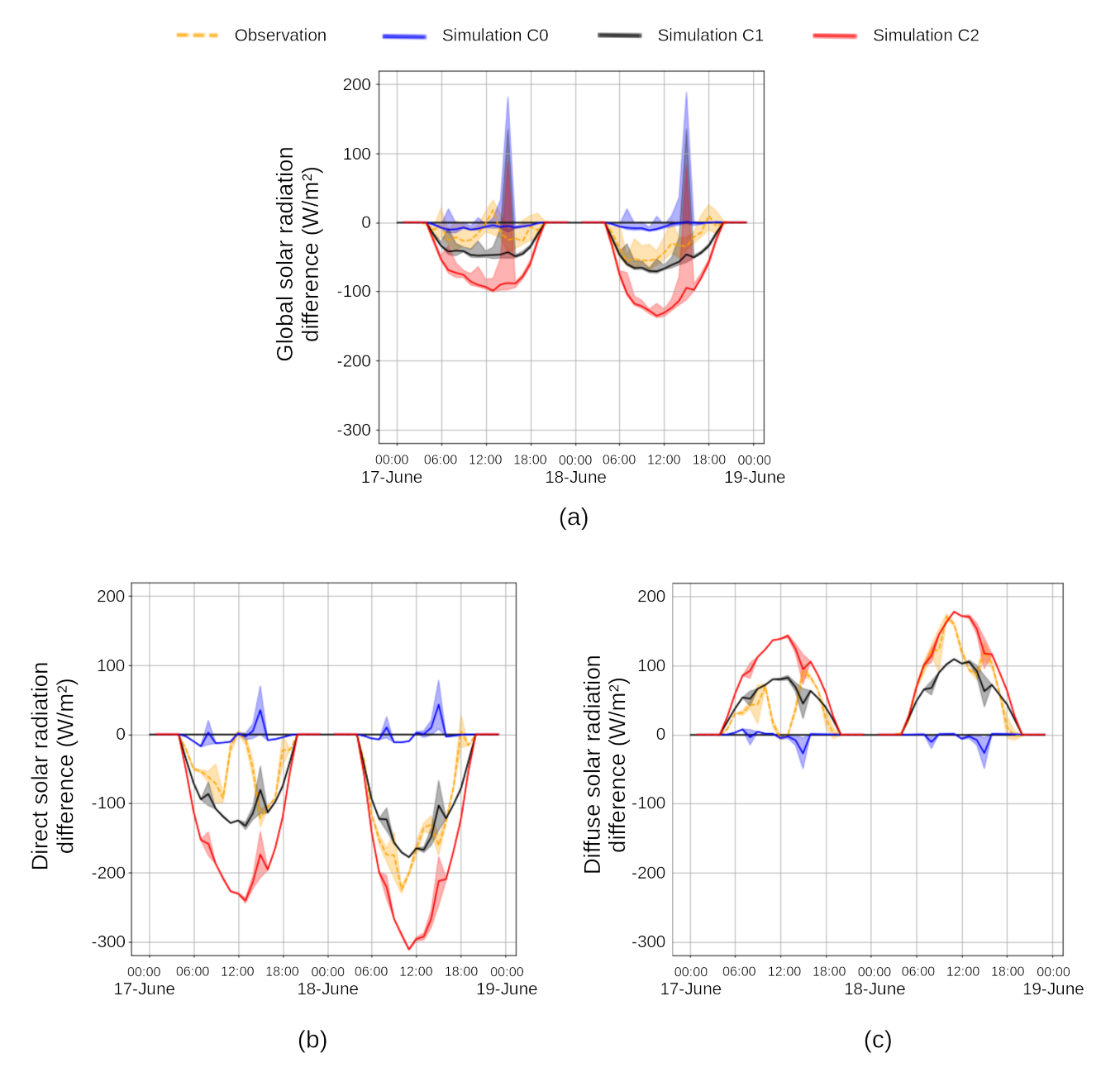


**Figure 7.** (a) global, (b) direct and (c) diffuse downward SW radiation difference for 17 and 18 June compared with 15 June. The mean value of the nine (two) global (direct and diffuse) SW radiation stations is represented by the line and is surrounded by a patch delineated at the bottom and at the top by the 0.1 and 0.9 quantiles respectively.





Although the simulations slightly underestimate the direct radiation decrease and the diffuse radiation increase, the effect of the aerosol on the solar radiation share between direct and diffuse radiation is rather accurately simulated for 18 June (Fig. 7b and Fig. 7c). Again, the sudden late morning peak for both direct and diffuse observed solar radiation is attributable to temporary clouds on 15 June.

The daily mean SW and LW radiation have the same order of magnitude (between 340 and 380 W/m<sup>2</sup> Tab. 1) but the average error of simulation C1 is slightly higher for the daily SW (+16 W/m<sup>2</sup>) than for the daily LW (-2.5 W/m<sup>2</sup>). However, the effect of dust aerosols on the daily mean downward infrared radiation is minor (-3 W/m<sup>2</sup> between C1 and C0 on the 18th), which makes these long-wave impacts negligible compared with solar radiation reduction (-31 W/m<sup>2</sup>).

**Table 1.** The daily average global solar radiation  $(W/m^2)$  observed and simulated at Palaiseau station. The numbers in brackets are the difference of solar radiation between a day and the reference day (15th June)

Date		2022-06-15	2022-06-16	2022-06-17	2022-06-18
Global solar radiation (W/m <sup>2</sup> )	Observation	350 (0)	352 (2)	338 (-12)	325 (-25)
	C0	369 (0)	371 (2)	367 (-2)	368 (-1)
	C1	369 (0)	370 (1)	345 (-24)	337 (-32)
	C2	369 (0)	369 (0)	323 (-46)	309 (-60)
Long-wave radiation (W/m <sup>2</sup> )	Observation	346	340	363	383
	C0	341	341	367	378
	C1	341	341	365	375
	C2	341	341	364	373

#### 210 3.3 Air temperature

#### 3.3.1 Near ground air temperature

The comparison of near-ground air temperature is performed for the 17 'rural' sites and for the single 'urban' site. When there is no aerosol plume in the atmosphere (15 June), the air temperature of almost all rural stations is overestimated by the model in the afternoon (about 1.75 K) but performs very well during the night (Fig. 8a). When explicitly considering the presence of aerosols, the model overestimation decreases in the afternoon for all simulations (on 18 June, the median error raises up to 5 K for C0 against 4 and 3 K for C1 and C2, respectively). The night-time simulated air temperature is also affected by the presence of aerosols: at midnight on 18 June, the median error is +2 K, +1.5K and +1 K for C0, C1 and C2, respectively. The same simulation error dynamic is observed for the urban station (Fig. 8b).



220

225



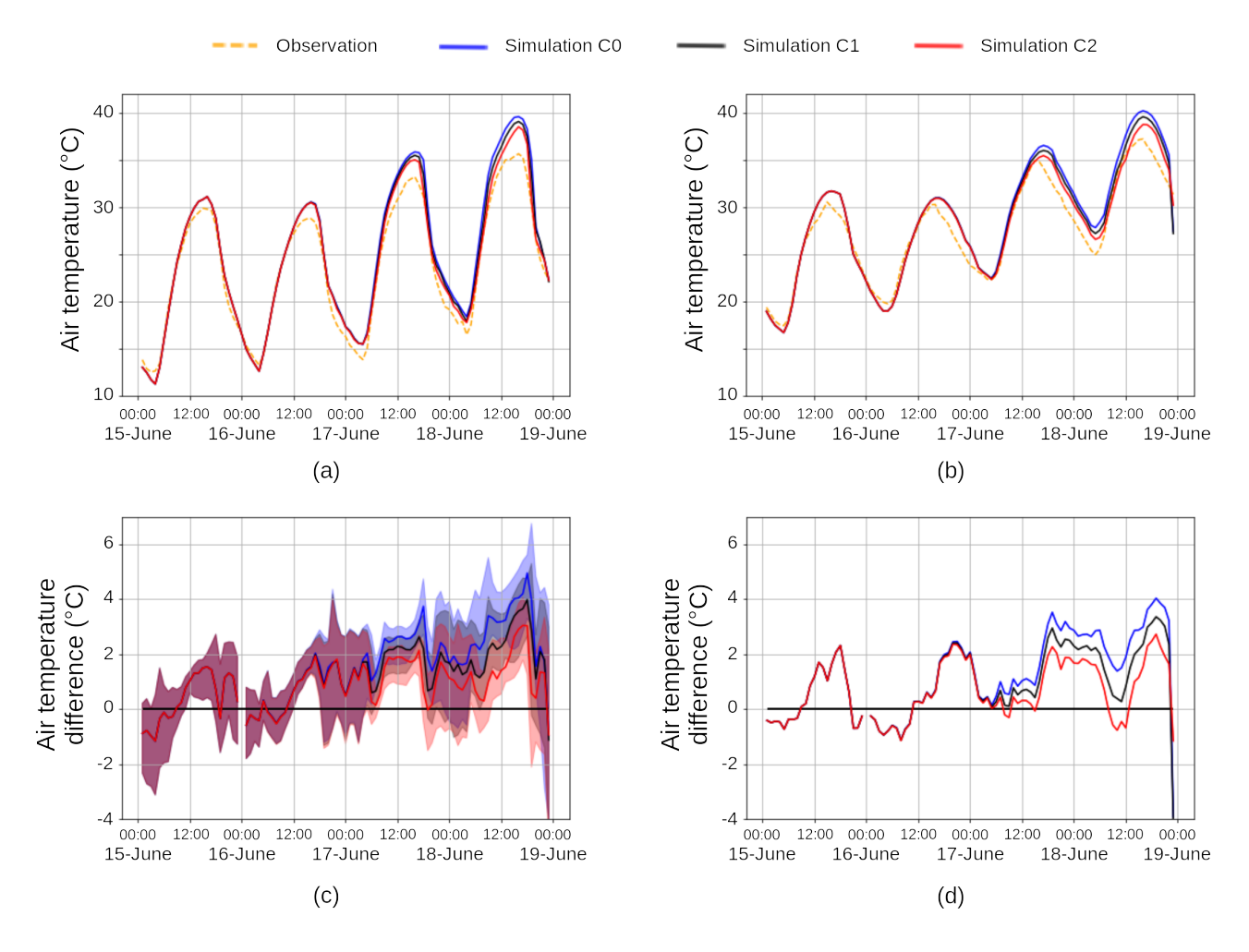


**Figure 8.** (a) Observed and simulated absolute air temperature and (c) difference between simulation and observation for rural stations. (b) Observed and simulated absolute air temperature and (d) difference between simulation and observation for the urban station. For rural stations, the median value of the 18 stations is represented by the line and is surrounded by a patch delineated at the bottom and at the top by the 0.1 and 0.9 quantiles respectively.

As for the solar radiation, the distinction between simulations with and without aerosols starts on 17 June and increases afterward. Overall, when aerosols are considered in the simulations, it clearly improves the performance of the model for the near-surface air temperature throughout the simulation period. More specifically, on the second half of the morning of 18 June, the C1 simulation difference with observation is nearly the same (about 0.5 K) as during the morning of 15 June (day without aerosol). This suggests that the effect of the aerosol on the air temperature (about 1 K decrease) is well simulated by the model. In the next section, the vertical structure of the boundary layer is further investigated to identify the reason for the near-ground air temperature bias of the model.



230

235

240

245



## 3.3.2 Upper atmosphere air temperature

The evaluation of the impact of dust aerosols on the vertical thermal structure of the atmosphere can be undertaken by comparing the simulation results with data from radiosonde and ceilometer measurements. The focus is on 18 June, during which four weather radiosondes were released from the inner part of Paris: at 00:00, 12:00, 16:00, and 20:00 (Fig. 9). At 00:00 UTC, the urban boundary layer (UBL) is well mixed and its height is well captured by all the simulations. The UBL temperature is slightly too warm, as in the residual layer up to 1000 m. This is likely remaining from the overestimation of the previous day air temperature (17 June, not shown). Above 1000 m, in the free atmosphere, the simulated profiles of temperature are similar and very good.

At 12:00 UTC, the differences in incoming solar radiation at the surface lead to different boundary layer heights. The best simulation here is C2. The C0 boundary layer height grows twice faster, while C1 is in the middle. This shows that the aerosols have a significant effect on the boundary layer development at this stage. During the afternoon (Fig. 9c), all three simulations produce a huge development of the boundary layer, contrary to the observations where the boundary layer extend remains limited, with a strong inversion. The turbulence and thermal schemes used by the Meso-NH model probably simulate a too strong entrainment rate at the top of the boundary layer or a slight temporal shift in the simulations of the large-scale structure change of the air mass that occurs in the evening, which could reduce the stability barrier in the free atmosphere. This strong entrainment causes the extra heating of the boundary layer and the surface (Fig. 8) during the afternoon. The simulations then overestimate the air temperature in the boundary layer, due to this too high extension of the boundary layer, resulting in the incorporation of warmer air from above. The 18 June afternoon is the period with the largest disagreement between the simulations and the observations. Still, there is an important role of the surface solar radiation reduction (due to the dust plume) in the dampening of the boundary layer development. At midnight, the nocturnal boundary layer reforms, and temperature differences between simulations are driven by the afternoon ones.





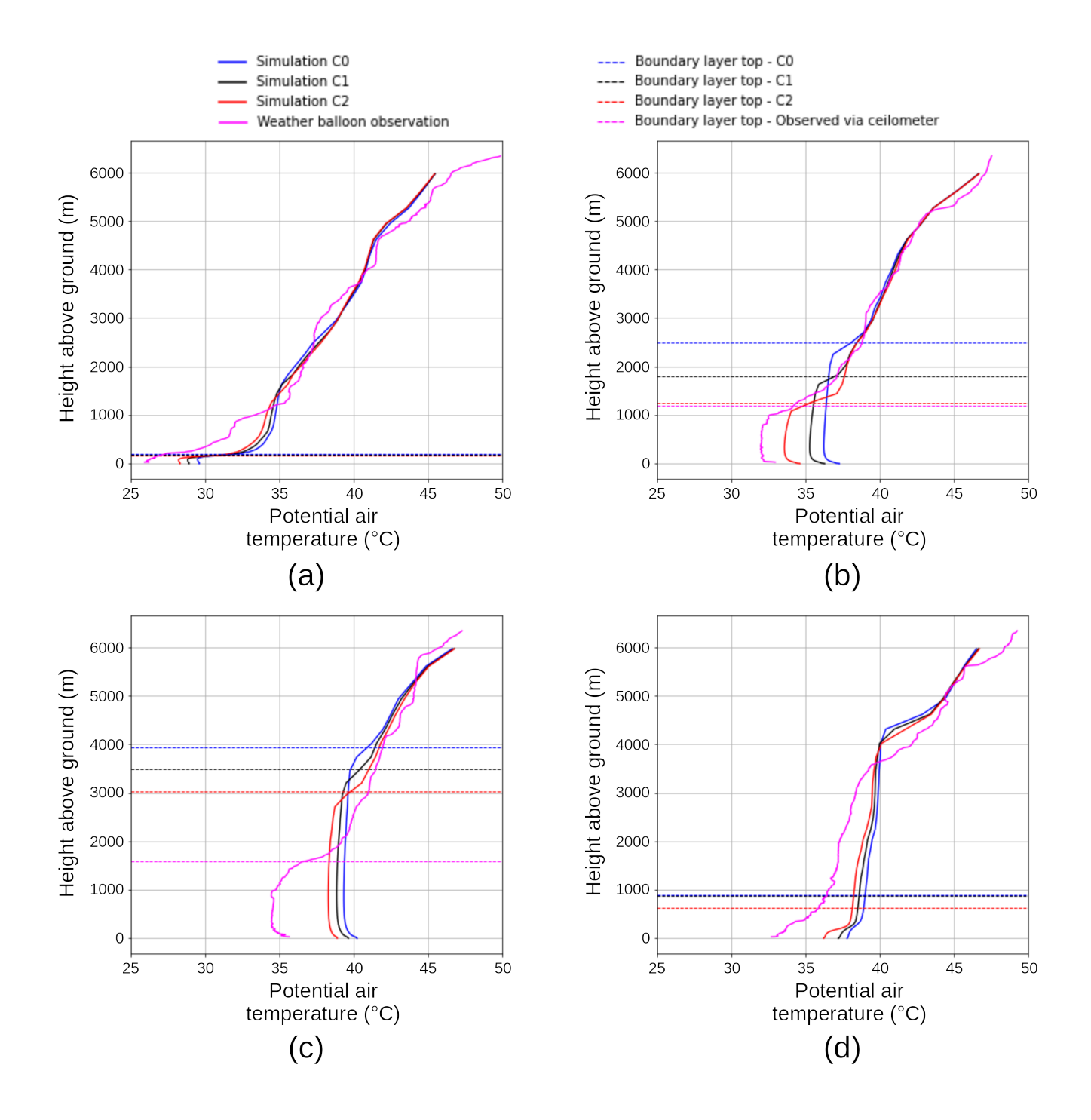


**Figure 9.** Potential air temperature profile simulated at the Jussieu station and observed using a radiosonde on 18 June at (a) 00:00, (b) 12:00, (c) 16:00 and (d) 20:00 UTC

.



250



The temporal evolution of the vertical structure of the atmosphere during the 3 days of the dust event is shown in Fig. 10. The model overestimates the boundary layer height (observed by the Jussieu station ceilometer), but this is improved in C1 simulation compared to C0. Comparison of the potential air temperature observed with the simulations at the Jussieu station confirms previous findings: for C1, during the two days with significant dust plume (17 and 18 June), there is a cooling of typically 0.5°C in the entire boundary layer compared to the simulation without dust.

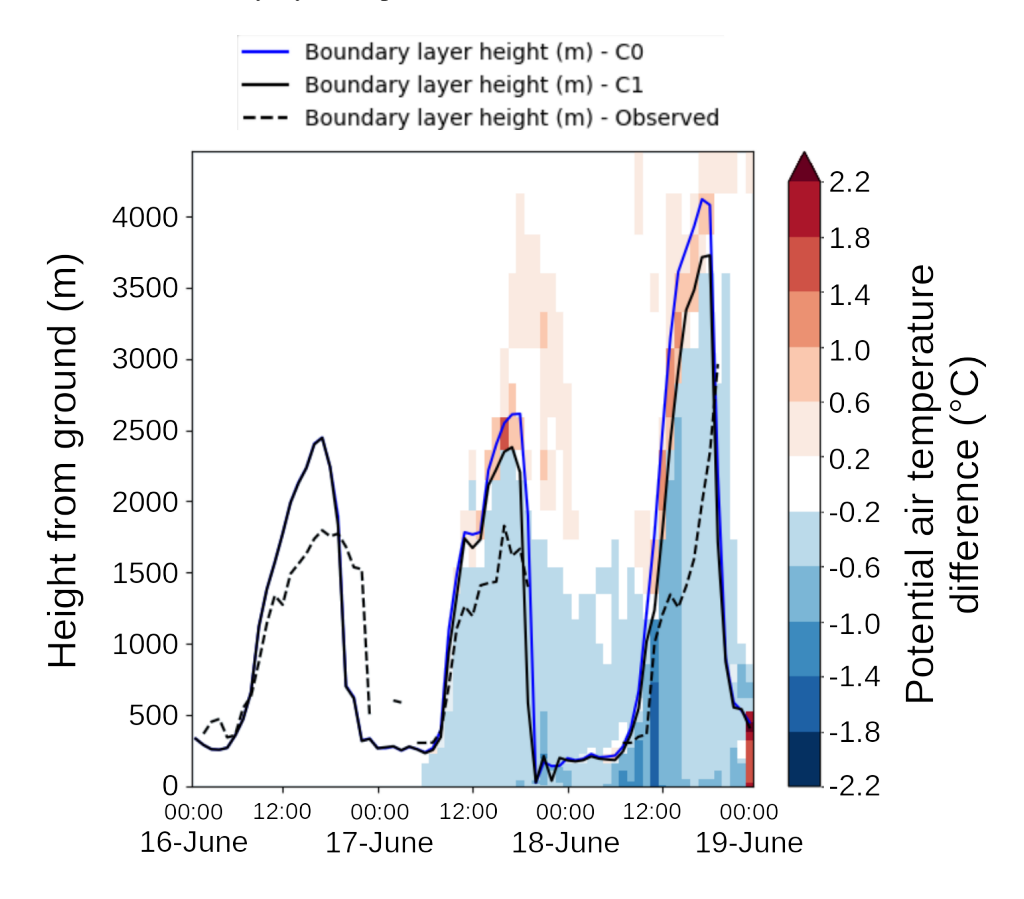


Figure 10. Vertical and temporal variation of potential air temperature difference between simulation C1 and C0 at the Jussieu station

## 3.4 Thermal comfort

255

The effect of aerosols on thermal comfort in urban areas is now being investigated. Previous sections showed that the effect of the aerosol on global, direct, and diffuse solar radiation was well predicted by simulation C1 (Sect. 3.2). The absolute values of both air temperature near the ground and boundary layer height were also improved when using this simulation (Sect. 3.3.1 and 3.3.2 respectively). Even if differences between observations and simulations remain, as for air temperature in the afternoon, we suppose that the differential effect of dust is of the correct order of magnitude, in particular because the radiation forcing impact is well simulated (section 3.2). To illustrate the effect of this specific dust aerosol event on thermal comfort, the





Universal Thermal Comfort Index (UTCI, Jendritzky et al., 2012) is calculated for simulations C0 and C1 and compared. The UTCI is a bioclimatic index that describes the physiological comfort of humans for specific meteorological conditions. It is expressed as a temperature and its calculation is based on an equation involving four meteorological variables: air temperature  $(T_a)$ , mean radiant temperature  $(T_{mrt})$ , air relative humidity (RH) and wind speed  $(U_{wind})$ . Equation (1), shows that UTCI can be seen as the air temperature plus an offset which depends on all variables (Błażejczyk et al., 2013):

265 UTCI = 
$$T_a$$
 + Offset( $T_a$ ,  $U_{wind}$ ,  $T_{mrt}$ ,  $RH$ ) (1)

Fig. 11a and Fig. 11b show the UTCI on 18 June simulated by C1 in the sun and in the shade, respectively. The results are averaged from 15:00 to 17:00 UTC. The choice of this time period is motivated by the fact that it is the warmest period of the day and a large number of people in France usually move from their workplace to their home during this time slot. The effect of aerosols on UTCI is investigated by calculating UTCI difference between C1 and C0 in the sun and in the shade (Fig. 11c and Fig. 11d, respectively). The increase of aerosol concentration in the atmosphere results in a slight decrease in UTCI values for the entire study area, although some contrasts are found: the decrease is more pronounced in the sun and in the city center (about 1°C) than in the shade and in the suburbs (about 0°C).





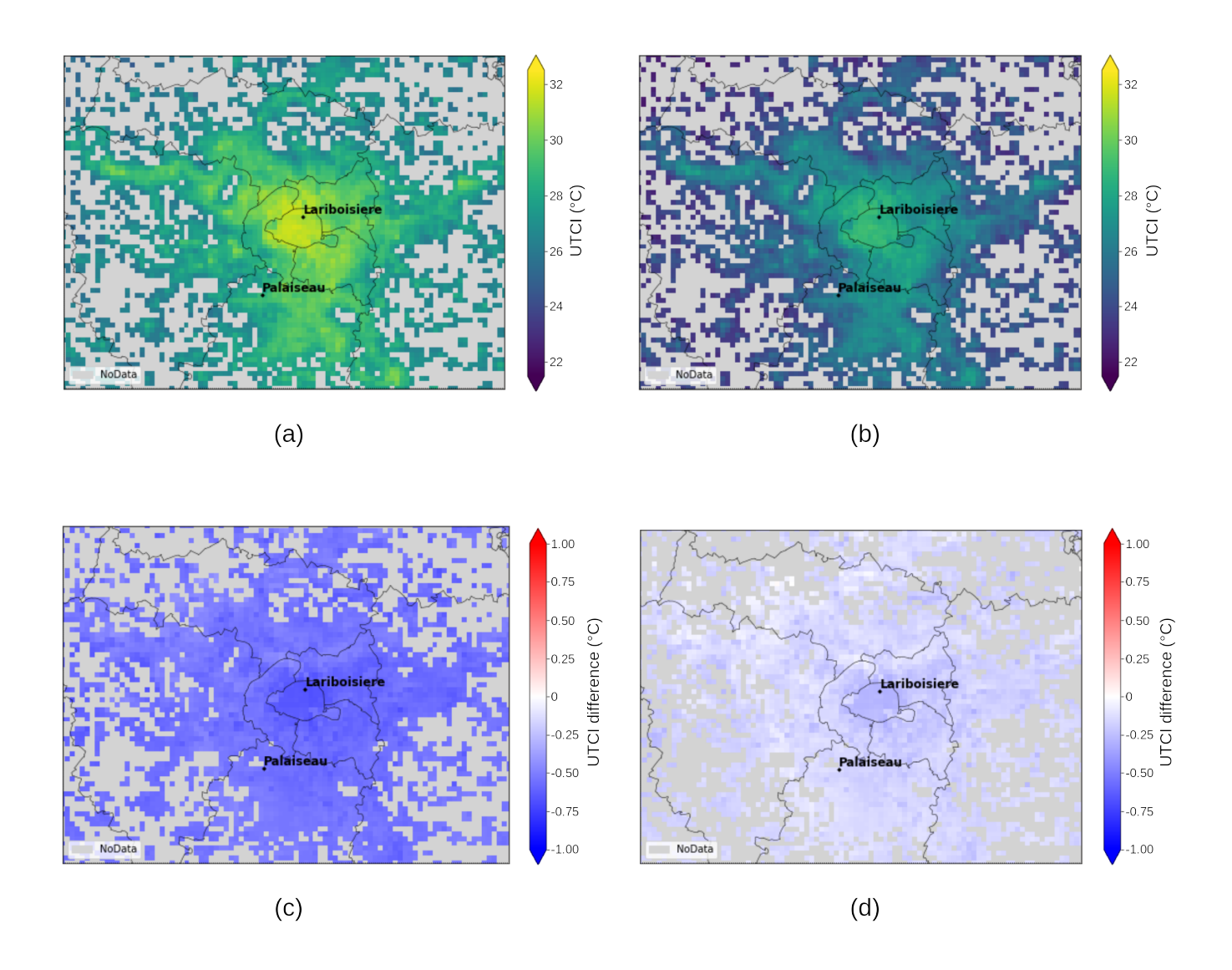


**Figure 11.** UTCI simulated by C1 in sun (a) and in shade (b). Difference between simulations C1 and C0 in sun (c) and shade (d). All plots are from 18 June and averaged from 15:00 UTC to 17:00 UTC

As shown in Sect. 3.3.1, the presence of dust aerosols decreases the near-surface air temperature for all stations located in the study area. The contribution of this variable can be removed in order to focus only on the UTCI offset term in the Eq. 1.

Then the results are more contrasted: the effect of aerosol is still negative in the sun (Fig. 12a) while it has a null or positive impact (up to 1.5°C) everywhere in the shade (Fig. 12b). The mean radiant temperature does not fully explain the effect of aerosol in the shade, as its effect is negative in the dense urban area (Paris city center, see Fig. 12d) while having a null UTCI offset (Fig. 12b). In this specific area, the slight decrease in wind speed (Fig. 12e) and the increase in relative humidity (Fig. 12f) compensate for the radiation effect. The decrease in wind speed has been previously documented in aerosol impact studies





(Péré et al., 2011) and is attributable to the decrease of turbulence in the shallower boundary layer, while the increase in relative humidity is the result of both the decrease in air temperature and a moister boundary layer (which did not incorporate much dry air through entrainment). On 18 June, the specific humidity of the C1 simulation shows slightly higher values than the C0 simulation (up to 0.4 g/kg of air at 4 pm, 0.2 g/kg at 10 am).





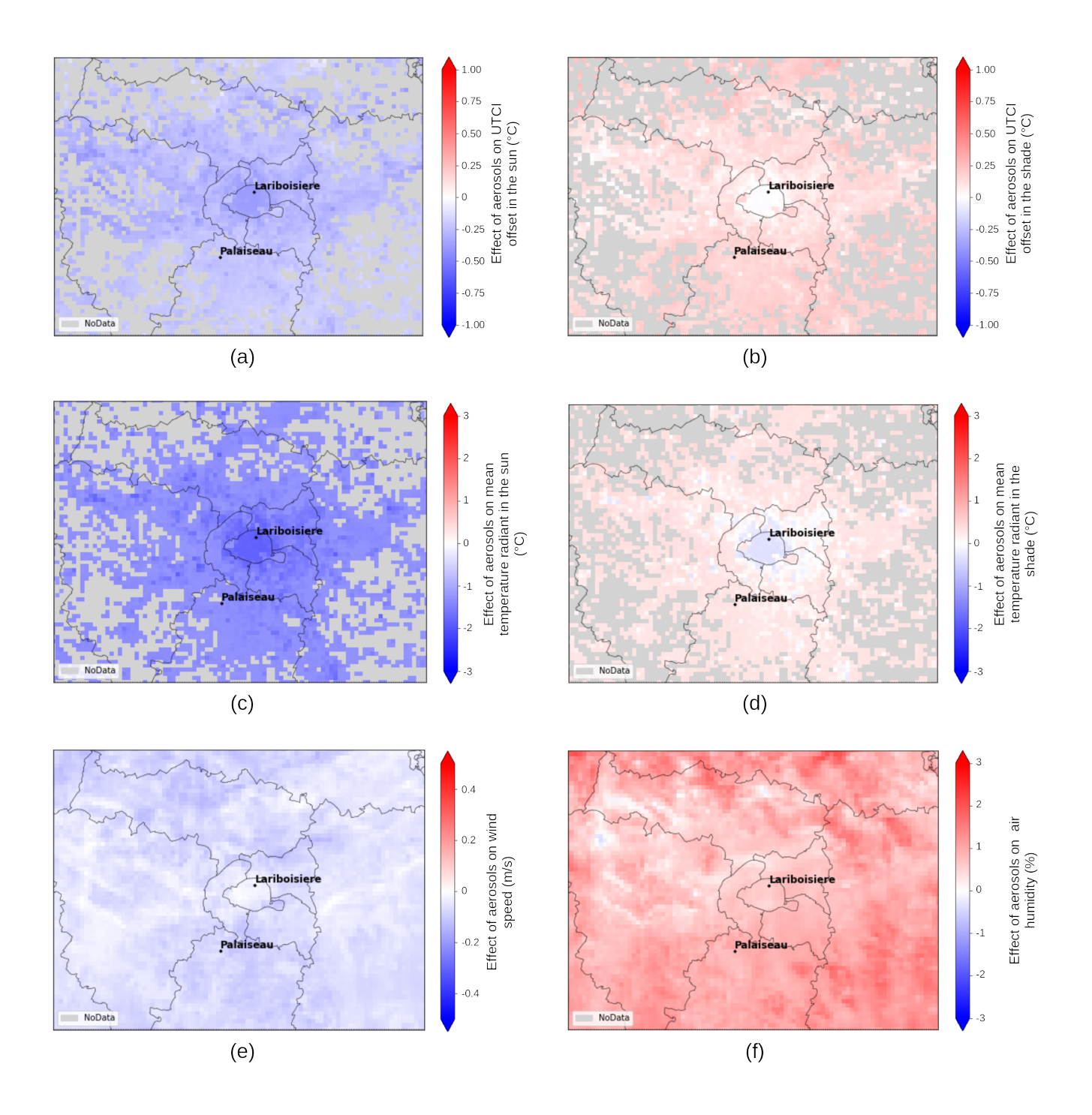


Figure 12. Difference between simulations C1 and C0 for (a) UTCI offset in sun, (b) UTCI offset in shade, (c)  $T_{mrt}$  in sun, (d)  $T_{mrt}$  in shade, (e) wind speed and (f) relative humidity



295

300



Two stations located in different environments are chosen to illustrate the temporal variability of the UTCI: Lariboisière and Palaiseau (see their location in Fig. 4). Lariboisière is the urban station. Its environment is composed of compact mid-rise buildings (Local Climate Zone (LCZ) type 2 - Stewart and Oke (2012)). Palaiseau, located south-west of Paris, includes many instruments. Its immediate environment is composed of sparse buildings (LCZ type 9). Note that the definition of each site is given using aggregated spatial information using the 1.2 km resolution grid cells.

Regardless of a person's location (in the shade or in the sun, at Lariboisière or Palaiseau), the aerosols generally decrease the values of both air temperature and UTCI and therefore improve the thermal comfort when compared to the simulation without aerosol. However, in the shade of sparsely built neighborhoods (Palaiseau), the UTCI offset, which is the thermal comfort contribution of all variables except air temperature, is worse with aerosols than without aerosols, reaching a maximum heating of up to 1.25°C at 10:00 UTC on 18 June (Fig. 13).

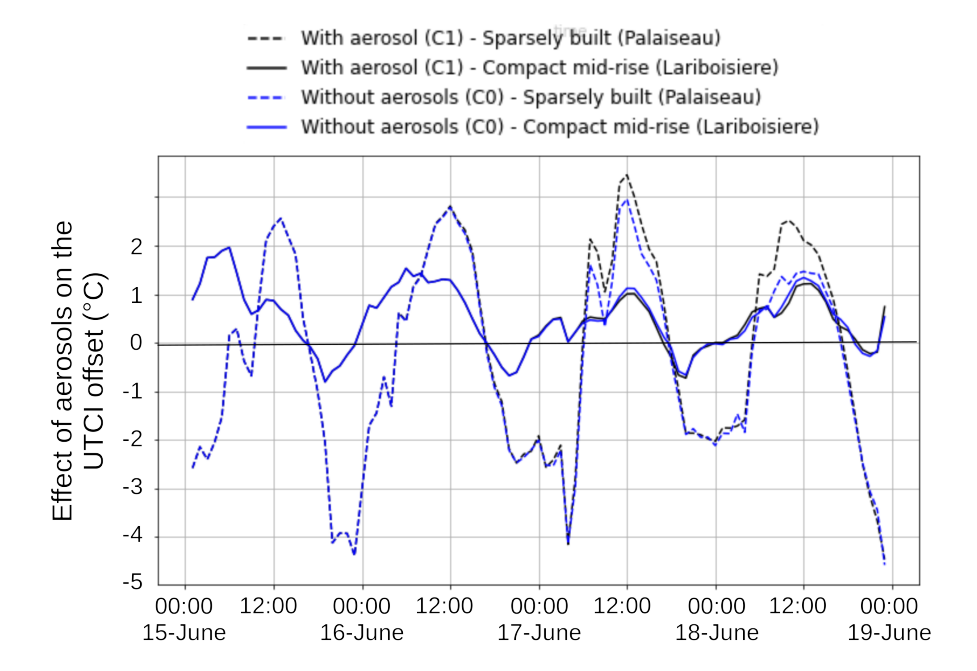


Figure 13. Temporal variation of the difference between UTCI in shade and air temperature for two sites for simulations C0 and C1

For that time, in Palaiseau, the differences in  $T_{mrt}$ , wind speed, and relative humidity between C1 and C0 are +1.5 °C, -1 m s<sup>-1</sup> and +3%, respectively (not shown). These effects almost compensated for the cooling due to the air temperature reduction and thus the presence of aerosol results in an almost no effect on thermal comfort (-0.2 °C). Seen from a different perspective, it also means that being in the shade in a suburban area with the level of aerosol observed on 18 June is equivalent, in terms of thermal comfort, to being in the shade with an aerosol-free atmosphere but with a 1.5 °C higher air temperature. To identify the contribution  $Contrib_i$  of each variable i to the effect of aerosols on UTCI, the following calculation, illustrated in Eq. 2



315

320



with the variable  $T_a$ , is performed for  $T_a$ ,  $T_{mrt}$ , RH,  $U_{wind}$ .

$$Contrib_{T_a} = UTCI(T_{a_{C_1}}, U_{wind_{C_0}}, T_{mrt_{C_0}}, RH_{C_0}) - UTCI(T_{a_{C_0}}, U_{wind_{C_0}}, T_{mrt_{C_0}}, RH_{C_0})$$
(2)

where the  $C_0$  and  $C_1$  subscripts refer to values in the C0 and C1 simulations.

Note that the full contribution of each variable can not be considered by this calculation, the UTCI equation defined by Jendritzky et al. (2012) having cross-contribution from each combination of two variables up to order 6. Thus, the sum of the individual contribution of each variable is not equal to the contribution of all variables at once, a residual term attributed to the cross-terms should be added (Eq. 3).

$$310 \quad UTCI_{C_1} - UTCI_{C_0} = Contrib_{T_a} + Contrib_{U_{wind}} + Contrib_{T_{mrt}} + Contrib_{RH} + Contrib_{cross-terms(T_a, U_{wind}, T_{mrt}, RH)}$$
(3)

Figure 14a shows the contribution of each meteorological variable to the effect of aerosols on UTCI. For the Palaiseau site, on 18 June at 10:00 UTC, apart from the air temperature impacting the UTCI negatively (-1.5 °C), all the variables contribute to increase the UTCI by 0.5 °C, 0.4 °C and 0.2 °C for the wind speed, the mean radiant temperature and the relative air humidity, respectively. This relative contribution order is only observed for this specific time and location: for the rest of the situations, the effect of the mean radiant temperature is larger in absolute value than the effect of wind speed and relative humidity (Fig. 14). As previously observed in Fig. 13, on 18 June, the location (urban versus suburban) has a larger impact at 10:00 than at 16:00 UTC: the effect of aerosol-induced reduction of UTCI is higher in Lariboisiere than in Palaiseau for any time of the day, but with greater importance at 10:00 (1.0 °C) than at 16:00 UTC (0.5 °C). In the afternoon, except for the mean radiant temperature, all variable contributions to UTCI are about the same for urban and suburban cases (Fig. 14b). Note that for all situations investigated here, the cross-term contribution has a rather low value.





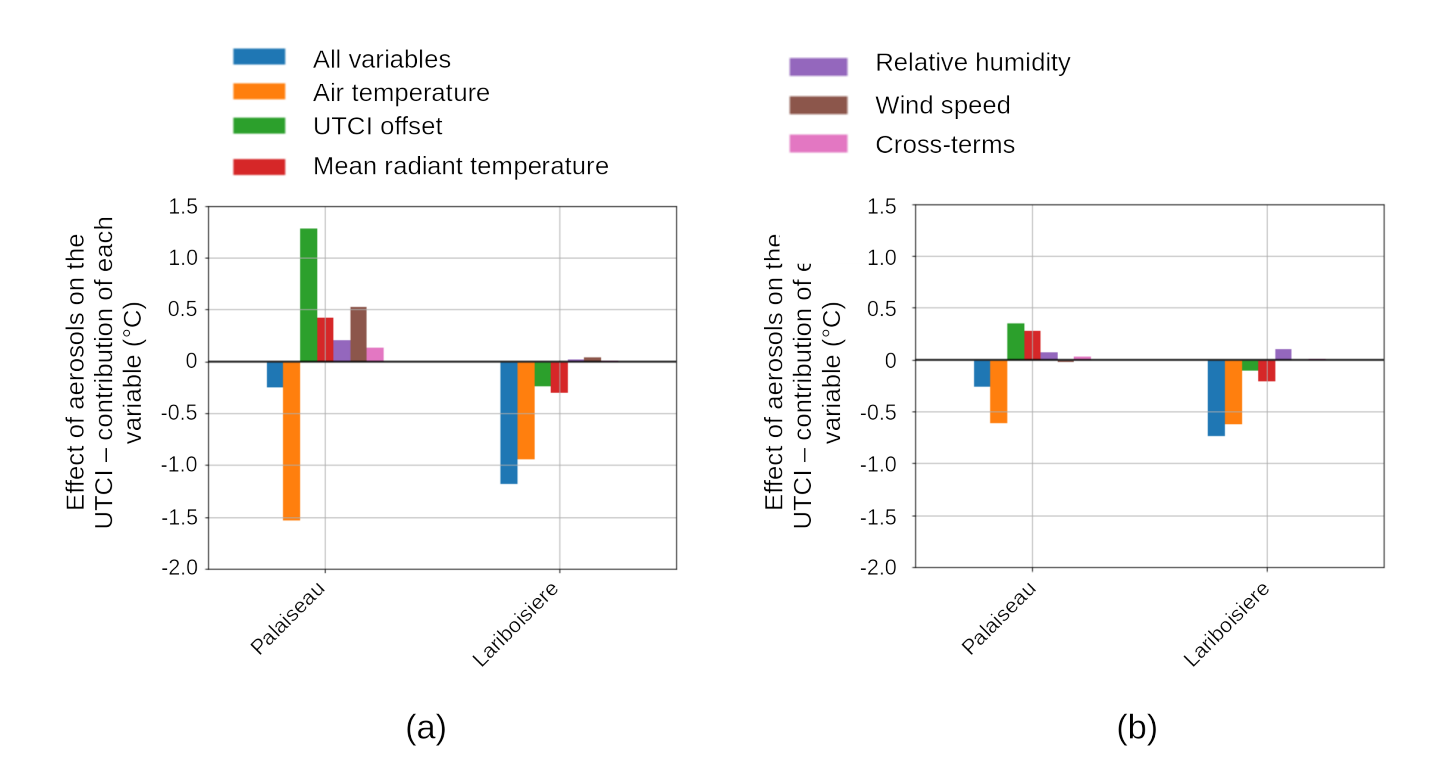


**Figure 14.** Contribution of each meteorological variable to the effect of aerosol on the UTCI on 18 June (a) at 10:00 UTC and (b) at 16:00 UTC

In summary, the presence of a dust plume during a heat wave contributes to reducing solar radiation and air temperature, leading to improved thermal comfort in sunlight, but no improvement in thermal comfort in suburban areas under shade.

# 4 Conclusions

325

330

To assess the potential impact of dust aerosols on urban thermal comfort, a case of strong heatwave over the Paris region, associated with an inter-continental Saharan dust outbreak, is investigated. Simulations without and with dust aerosols are first validated against extensive observations of the PANAME-Urban experimental campaign. The simulations perform correctly, the results being consistent with observations, except the afternoon of the last day of the event being slightly overheated. This difference is mainly explained by the faster decrease of the AOD in the observations than in the simulations. Using the CAMS explicit dust aerosol fields in the simulations improves the results in all aspects. The impact of aerosols on incoming shortwave radiation is strong (up to a mean daily effect of -31 W/m²), leading to shallower boundary layers and cooler temperatures, both at ground level and within the atmospheric boundary layer. The impact on thermal comfort is hence mainly driven by the air temperature, with improved thermal comfort sensation due to the dust aerosol impact. However, in the shadow of suburban areas (open low-rise neighborhoods), the increased diffuse radiation, along with the lower wind speed and higher relative humidity, almost counterbalances the cooling effect due to air temperature.



335

340

345

350

355

360

365



While the total impact on thermal comfort is neutral for this specific area and meteorological event, this may be different under other conditions. Various factors and processes can influence this result, but the literature dedicated to effect of aerosol on thermal comfort is very limited. Obviously, the variability in radiative effects due to aerosol properties and distribution is a key component. But for a same AOD value, two events may have quite different radiation impacts. Logothetis et al. (2021) have used the worldwide available AERONET data to highlight that for a same AOD value, the decrease in solar radiation at the bottom of the atmosphere is more important for fine particles than for coarse ones. Kaskaoutis et al. (2016) have also shown that the diffuse-direct irradiance ratio is higher for fine particles than for coarse particles. To determine the effect of aerosols on the other climate variables is even more complex. For example, the near-surface air temperature depends on the previously discussed incident solar flux but also on sensible and latent heat fluxes emitted by the terrestrial surface, on aerosol solar absorption near the ground and on atmospheric circulation (Péré et al., 2011). During the 7 to 15 August 2003 heat wave in Western Europe, a large amount of primary and secondary aerosols were emitted to the atmosphere and were associated to a large concentration of ozone. In the South of France, the mean solar radiation received at the surface was 30 W/m<sup>2</sup> lower than without aerosols, resulting in a 0.3 K decrease in near-surface air temperature (Péré et al., 2011). The same level of AOD (about 0.6 on 18 June 2022) and similar effect on the solar radiation (-32 W/m<sup>2</sup>) were observed in our case, but the air temperature decrease was more important (1 K). In Spain, for the same 2003 heat wave event, the near surface air temperature decrease was the same as in Southern France (0.3 K) whereas the aerosol impact on solar radiation was twice lower (-15 W/m<sup>2</sup>). Thus a difference of location or period of the year, of aerosol type, size, concentration or aerosol distribution within the atmosphere level may lead to considerable differences on the four meteorological variables (air temperature, mean radiant temperature, wind speed and air relative humidity) used to estimate the thermal comfort via the UTCI indicator.

The results presented in this study show that realistic consideration of atmospheric aerosols in weather forecasting models is essential for accurate prediction of heat exposure conditions in cities. In the present case study, certain insights into urban comfort conditions during desert dust plume events have been revealed. Nevertheless, the complexity of the radiation processes at play within the urban canopy and the feedbacks on local climate variables make it difficult to generalize these conclusions. Future work could study the influence of other types of aerosols on weather conditions and thermal comfort. This would be particularly relevant for aerosols emitted from cities inside the boundary layer. Another research direction could be to evaluate the impact of more intense dust episodes in cities nearby emission source areas, such as Athens in Greece, or Dakar in Senegal, both closer to the Sahara desert.

Data availability. All raw observational data are available from the AERIS data centre catalogue at https://paname.aeris-data.fr/data-catalogue-2/.

Author contributions. JB has performed the simulations and analyses and contributed to all stages of the paper writing. TN performed the simulations, and contributed to the analyses and writing of the paper. VM coordinated the project proposal for CNRM, supervised the study,





and contributed to the analyses and the writing of the paper. AL contributed to the analyses and reviewed the final draft of the paper. JW and QR provided support for the simulations and reviewed the final draft of the paper. PT contributed as expert in aerosols modeling and revised the final draft of the paper.

Competing interests. The authors declare that they have no conflict of interest.

370 Acknowledgements. We gratefully acknowledge the support and funding from the EU Action 2021-2-29 User-centric Assessment of Climate Change Impacts for Adaptation [U-CLIMADAPT] under Grant Agreement No 2022/SI2.879178 and SI2.879180/ SGA 20 implementing the FPA 275/G/GRO/COPE/17/10042. We would like to thank Alejandra Velazquez-Garcia and Cyrielle Deanjean as well as Simone Kotthaus for the helpful discussions on dust transport and boundary layer height, respectively.





#### References

380

- Bangert, M., Nenes, A., Vogel, B., Vogel, H., Barahona, D., Karydis, V. A., Kumar, P., Kottmeier, C., and Blahak, U.: Saharan dust event impacts on cloud formation and radiation over Western Europe, Atmospheric Chemistry and Physics, 12, 4045–4063, https://doi.org/10.5194/acp-12-4045-2012, publisher: Copernicus GmbH, 2012.
  - Basart, S., Nickovic, S., Terradellas, E., Cuevas, E., García-Pando, C. P., García-Castrillo, G., Werner, E., and Benincasa, F.: The WMO SDS-WAS Regional Center for Northern Africa, Middle East and Europe, E3S Web of Conferences, 99, 04008, https://doi.org/10.1051/e3sconf/20199904008, publisher: EDP Sciences, 2019.
  - Bernstein, D. N., Neelin, J. D., Li, Q. B., and Chen, D.: Could aerosol emissions be used for regional heat wave mitigation?, Atmospheric Chemistry and Physics, 13, 6373–6390, https://doi.org/10.5194/acp-13-6373-2013, 2013.
  - Błażejczyk, K., Jendritzky, G., Bröde, P., Fiala, D., Havenith, G., Epstein, Y., Psikuta, A., and Kampmann, B.: An introduction to the universal thermal climate index (UTCI), Geographia Polonica, 86, 5–10, 2013.
- Boone, A., Samuelsson, P., Gollvik, S., Napoly, A., Jarlan, L., Brun, E., and Decharme, B.: The interactions between soil-biosphere–atmosphere land surface model with a multi-energy balance (ISBA-MEB) option in SURFEXv8–Part 1: Model description, Geoscientific Model Development, 10, 843–872, https://doi.org/10.5194/gmd-10-843-2017, 2017.
  - Brousseau, P., Seity, Y., Ricard, D., and Léger, J.: Improvement of the forecast of convective activity from the AROME-France system, Quarterly Journal of the Royal Meteorological Society, 142, 2231–2243, 2016.
- 390 Cuxart, J., Bougeault, P., and Redelsperger, J.-L.: A turbulence scheme allowing for mesoscale and large-eddy simulations, Quarterly Journal of the Royal Meteorological Society, 126, 1–30, https://doi.org/10.1002/qj.49712656202, \_eprint: https://rmets.onlinelibrary.wiley.com/doi/pdf/10.1002/qj.49712656202, 2000.
  - Córdoba-Jabonero, C., Sicard, M., López-Cayuela, M.-, Ansmann, A., Comerón, A., Zorzano, M.-P., Rodríguez-Gómez, A., and Muñoz-Porcar, C.: Aerosol radiative impact during the summer 2019 heatwave produced partly by an inter-continental Saharan dust outbreak Part 1: Short-wave dust direct radiative effect, Atmospheric Chemistry and Physics, 21, 6455–6479, https://doi.org/10.5194/acp-21-6455-
  - 2021, 2021.

- Decharme, B., Boone, A., Delire, C., and Noilhan, J.: Local evaluation of the Interaction between Soil Biosphere Atmosphere soil multilayer diffusion scheme using four pedotransfer functions, Journal of Geophysical Research: Atmospheres, 116, https://doi.org/10.1029/2011JD016002, 2011.
- Forster, A., Augros, C., and Masson, V.: Urban influence on convective precipitation in the Paris region: Hectometric ensemble simulations in a case study, Quarterly Journal of the Royal Meteorological Society, 150, 3028–3051, https://doi.org/10.1002/qj.4749, 2024.
  - Fouquart, Y.: Computations of solar heating of the Earth's atmosphere: A new parameterization, Beitraege zur Physik der Atmosphaere, 53, 35, 1980.
- Grini, A., Tulet, P., and Gomes, L.: Dusty weather forecasts using the MesoNH mesoscale atmospheric model, Journal of Geophysical

  Research: Atmospheres, 111, 2006.
  - Hersbach, H., Bell, B., Berrisford, P., Biavati, G., Horányi, A., Muñoz Sabater, J., Nicolas, J., Peubey, C., Radu, R., Rozum, I., et al.: ERA5 hourly data on pressure levels from 1940 to present, Copernicus climate change service (c3s) climate data store (cds), 10, 24381, 2023.
  - Hoarau, T., Barthe, C., Tulet, P., Claeys, M., Pinty, J.-P., Bousquet, O., Delanoë, J., and Vié, B.: Impact of the generation and activation of sea salt aerosols on the evolution of Tropical Cyclone Dumile, Journal of Geophysical Research: Atmospheres, 123, 8813–8831, 2018.



420

425

435



- 410 Hodnebrog, Ø., Myhre, G., Jouan, C., Andrews, T., Forster, P. M., Jia, H., Loeb, N. G., Olivié, D. J., Paynter, D., Quaas, J., et al.: Recent reductions in aerosol emissions have increased Earth's energy imbalance, Communications Earth & Environment, 5, 166, 2024.
  - Holben, B. N., Eck, T. F., Slutsker, I., Tanré, D., Buis, J. P., Setzer, A., Vermote, E., Reagan, J. A., Kaufman, Y. J., Nakajima, T., Lavenu, F., Jankowiak, I., and Smirnov, A.: AERONET—A Federated Instrument Network and Data Archive for Aerosol Characterization, Remote Sensing of Environment, 66, 1–16, https://doi.org/10.1016/S0034-4257(98)00031-5, 1998.
- Honnert, R., Masson, V., Lac, C., and Nagel, T.: A theoretical analysis of mixing length for atmospheric models from micro to large scales, Frontiers in Earth Science, 8, 582 056, 2021.
  - Inness, A., Ades, M., Agustí-Panareda, A., Barré, J., Benedictow, A., Blechschmidt, A.-M., Dominguez, J. J., Engelen, R., Eskes, H., Flemming, J., et al.: The CAMS reanalysis of atmospheric composition, Atmospheric Chemistry and Physics, 19, 3515–3556, 2019.
  - Jendritzky, G., De Dear, R., and Havenith, G.: UTCI—why another thermal index?, International journal of biometeorology, 56, 421–428, 2012.
  - Kaskaoutis, D., Kambezidis, H., Dumka, U., and Psiloglou, B.: Dependence of the spectral diffuse-direct irradiance ratio on aerosol spectral distribution and single scattering albedo, Atmospheric Research, 178, 84–94, 2016.
  - Kotthaus, S., Haeffelin, M., Drouin, M.-A., Dupont, J.-C., Grimmond, S., Haefele, A., Hervo, M., Poltera, Y., and Wiegner, M.: Tailored Algorithms for the Detection of the Atmospheric Boundary Layer Height from Common Automatic Lidars and Ceilometers (ALC), Remote Sensing, 12, https://doi.org/10.3390/rs12193259, 2020.
  - Lac, C., Chaboureau, J.-P., Masson, V., Pinty, J.-P., Tulet, P., Escobar, J., Leriche, M., Barthe, C., Aouizerats, B., Augros, C., et al.: Overview of the Meso-NH model version 5.4 and its applications, Geoscientific Model Development, 11, 1929–1969, https://doi.org/10.5194/gmd-11-1929-2018, 2018.
- LeGrand, S. L., Polashenski, C., Letcher, T. W., Creighton, G. A., Peckham, S. E., and Cetola, J. D.: The AFWA dust emission scheme for the GOCART aerosol model in WRF-Chem v3.8.1, Geoscientific Model Development, 12, 131–166, https://doi.org/10.5194/gmd-12-131-2019, publisher: Copernicus GmbH, 2019.
  - Lemonsu, A., Barrau, S., Capo, J., Céspedes, J., Dahech, S., de Munck, C., Dumas, G., Jean-Charles, D., Dupuis, V., Etienne, J.-C., Garrouste, O., Goret, M., Haeffelin, M., Keravec, P., Kotthaus, S., Madelin, M., Martinet, P., Masson, V., Nagel, T., Price, J., Ribaud, J.-F., Rivollet, M., Roberts, G., Roy, A., Unger, V., Wilson, R., Wallois, S., and Wurtz, J.: PANAME-Urban campaign: investigating multiscale surface-atmosphere interactions and thermal-contrasts in the Paris region (France), Bulletin of the American Meteorological Society, pp. XX–XX, under rev.
  - Logothetis, S.-A., Salamalikis, V., and Kazantzidis, A.: The impact of different aerosol properties and types on direct aerosol radiative forcing and efficiency using AERONET version 3, Atmospheric Research, 250, 105 343, 2021.
- Lunet, T., Lac, C., Auguste, F., Visentin, F., Masson, V., and Escobar, J.: Combination of WENO and explicit Runge–Kutta methods for wind transport in the Meso-NH model, Monthly Weather Review, 145, 3817–3838, 2017.
  - Masson, V.: A physically-based scheme for the urban energy budget in atmospheric models, Boundary-layer meteorology, 94, 357–397, 2000.
  - Masson, V., Le Moigne, P., Martin, E., Faroux, S., Alias, A., Alkama, R., Belamari, S., Barbu, A., Boone, A., Bouyssel, F., et al.: The SURFEXv7. 2 land and ocean surface platform for coupled or offline simulation of earth surface variables and fluxes, Geoscientific Model Development, 6, 929–960, https://doi.org/10.5194/gmd-6-929-2013, 2013.
  - Masson, V., Lemonsu, A., Hidalgo, J., and Voogt, J.: Urban climates and climate change, Annual Review of Environment and Resources, 45, 411–444, 2020.





- Mlawer, E. J., Taubman, S. J., Brown, P. D., Iacono, M. J., and Clough, S. A.: Radiative transfer for inhomogeneous atmospheres: RRTM, a validated correlated-k model for the longwave, Journal of Geophysical Research: Atmospheres, 102, 16663–16682, 1997.
- Noilhan, J. and Planton, S.: A simple parameterization of land surface processes for meteorological models, Monthly weather review, 117, 536–549, 1989.
  - Oke, T. R., Mills, G., Christen, A., and Voogt, J. A.: Urban climates, Cambridge university press, 2017.
  - Oke, T. R. et al.: Initial guidance to obtain representative meteorological observations at urban sites, vol. 81, World Meteorological Organization Geneva, 2004.
- Park, S.-U., Ahn, H.-J., and Park, M.-S.: Direct shortwave radiative forcing of the Asian dust aerosol on dust emission, Theoretical and Applied Climatology, 101, 179–190, https://doi.org/10.1007/s00704-009-0245-3, 2010.
  - Pergaud, J., Masson, V., Malardel, S., and Couvreux, F.: A parameterization of dry thermals and shallow cumuli for mesoscale numerical weather prediction, Boundary-layer meteorology, 132, 83–106, 2009.
  - Pinty, J.-P. and Jabouille, P.: A mixed-phase cloud parameterization for use in mesoscale non-hydrostatic model: simulations of a squall line and of orographic precipitations, in: Conf. on cloud physics, pp. 217–220, Amer. Meteor. Soc. Everett, WA, 1998.
  - Péré, J. C., Mallet, M., Pont, V., and Bessagnet, B.: Impact of aerosol direct radiative forcing on the radiative budget, surface heat fluxes, and atmospheric dynamics during the heat wave of summer 2003 over western Europe: A modeling study: AEROSOL DIRECT RADIATIVE IMPACTS, Journal of Geophysical Research: Atmospheres, 116, n/a–n/a, https://doi.org/10.1029/2011JD016240, 2011.
- Redon, E., Lemonsu, A., and Masson, V.: An urban trees parameterization for modeling microclimatic variables and thermal comfort conditions at street level with the Town Energy Balance model (TEB-SURFEX v8. 0), Geoscientific Model Development, 13, 385–399, https://doi.org/10.5194/gmd-13-385-2020, 2020.
  - Redon, E. C., Lemonsu, A., Masson, V., Morille, B., and Musy, M.: Implementation of street trees within the solar radiative exchange parameterization of TEB in SURFEX v8. 0, Geoscientific Model Development, 10, 385–411, https://doi.org/10.5194/gmd-10-385-2017, 2017.
- 470 Rémy, S., Kipling, Z., Huijnen, V., Flemming, J., Nabat, P., Michou, M., Ades, M., Engelen, R., and Peuch, V.-H.: Description and evaluation of the tropospheric aerosol scheme in the Integrated Forecasting System (IFS-AER, cycle 47R1) of ECMWF, Geoscientific Model Development, 15, 4881–4912, https://doi.org/10.5194/gmd-15-4881-2022, 2022.
  - Riette, S.: Development of "Physical Parametrizations with PYthon" (PPPY, version 1.1) and its usage to reduce the time-step dependency in a microphysical scheme, Geoscientific Model Development, 13, 443–460, 2020.
- Schepanski, K.: Transport of Mineral Dust and Its Impact on Climate, Geosciences, 8, 151, https://doi.org/10.3390/geosciences8050151, 2018.
  - Schoetter, R., Kwok, Y. T., de Munck, C., Lau, K. K. L., Wong, W. K., and Masson, V.: Multi-layer coupling between SURFEX-TEB-v9. 0 and Meso-NH-v5. 3 for modelling the urban climate of high-rise cities, Geoscientific Model Development, 13, 5609–5643, https://doi.org/10.5194/gmd-13-5609-2020, 2020.
- 480 Seity, Y., Brousseau, P., Malardel, S., Hello, G., Bénard, P., Bouttier, F., Lac, C., and Masson, V.: The AROME-France convective-scale operational model, Monthly Weather Review, 139, 976–991, 2011.
  - Skamarock, W. C., Klemp, J. B., Dudhia, J., Gill, D. O., Barker, D. M., Wang, W., and Powers, J. G.: A description of the advanced research WRF version 2, Tech. rep., NCAR, 2005.





- Sofiev, M., Vira, J., Kouznetsov, R., Prank, M., Soares, J., and Genikhovich, E.: Construction of the SILAM Eulerian atmospheric dispersion model based on the advection algorithm of Michael Galperin, Geoscientific Model Development, 8, 3497–3522, https://doi.org/10.5194/gmd-8-3497-2015, publisher: Copernicus GmbH, 2015.
  - Stewart, I. D. and Oke, T. R.: Local climate zones for urban temperature studies, Bulletin of the American Meteorological Society, 93, 1879–1900, 2012.
- Stocker, T. F., Qin, D., Plattner, G.-K., Tignor, M. M. B., Allen, S. K., Boschung, J., Nauels, A., Xia, Y., Bex, V., Midgley, P. M., Alexander,
  L. V., Allen, S. K., Bindoff, N. L., Breon, F.-M., Church, J. A., Cubasch, U., Emori, S., Forster, P., Friedlingstein, P., Gillett, N., Gregory,
  J. M., Hartmann, D. L., Jansen, E., Kirtman, B., Knutti, R., Kumar Kanikicharla, K., Lemke, P., Marotzke, J., Masson-Delmotte, V.,
  Meehl, G. A., Mokhov, I. I., Piao, S., Plattner, G.-K., Dahe, Q., Ramaswamy, V., Randall, D., Rhein, M., Rojas, M., Sabine, C., Shindell,
  D., Stocker, T. F., Talley, L. D., Vaughan, D. G., Xie, S.-P., Allen, M. R., Boucher, O., Chambers, D., Hesselbjerg Christensen, J., Ciais,
  P., Clark, P. U., Collins, M., Comiso, J. C., Vasconcellos de Menezes, V., Feely, R. A., Fichefet, T., Fiore, A. M., Flato, G., Fuglestvedt,
  J., Hegerl, G., Hezel, P. J., Johnson, G. C., Kaser, G., Kattsov, V., Kennedy, J., Klein Tank, A. M. G., Le Quere, C., Myhre, G., Osborn,
  T., Payne, A. J., Perlwitz, J., Power, S., Prather, M., Rintoul, S. R., Rogelj, J., Rusticucci, M., Schulz, M., Sedlacek, J., Stott, P. A., Sutton,
  R., Thorne, P. W., and Wuebbles, D.: Climate Change 2013. The Physical Science Basis. Working Group I Contribution to the Fifth
  Assessment Report of the Intergovernmental Panel on Climate Change Abstract for decision-makers; Changements climatiques 2013.
  Les elements scientifiques. Contribution du groupe de travail I au cinquieme rapport d'evaluation du groupe d'experts intergouvernemental
  sur l'evolution du CLIMAT Resume a l'intention des decideurs, https://www.osti.gov/etdeweb/biblio/22221318, 2013.
  - Tardieu, J. and Leroy, M.: Radome, le réseau temps réel d'observation au sol de Météo-France, La Météorologie, 2003, 40-43, 2003.
  - Tegen, I., Hollrig, P., Chin, M., Fung, I., Jacob, D., and Penner, J.: Contribution of different aerosol species to the global aerosol extinction optical thickness: Estimates from model results, Journal of Geophysical Research: Atmospheres, 102, 23 895–23 915, 1997.
  - Tulet, P., Mallet, M., Pont, V., Pelon, J., and Boone, A.: The 7–13 March 2006 dust storm over West Africa: Generation, transport, and vertical stratification, Journal of Geophysical Research: Atmospheres, 113, 2008.
  - Wang, Z., Xue, L., Liu, J., Ding, K., Lou, S., Ding, A., Wang, J., and Huang, X.: Roles of Atmospheric Aerosols in Extreme Meteorological Events: a Systematic Review, Current Pollution Reports, 8, 177–188, https://doi.org/10.1007/s40726-022-00216-9, 2022.
  - Wiki CNRM: Wiki ECOCLIMAP-SG CNRM Open Source Site. Retrieved from https://opensource.umr-cnrm.fr/projects/ecoclimap-sg/wiki. Accessed 20 february 2025., 2018.
- Wurtz, J., Bouniol, D., and Vié, B.: Improvements to the parametrization of snow in AROME in the context of ice crystal icing, Quarterly Journal of the Royal Meteorological Society, 2023.
  - Zhang, Y., Wen, X. Y., and Jang, C. J.: Simulating chemistry–aerosol–cloud–radiation–climate feedbacks over the continental U.S. using the online-coupled Weather Research Forecasting Model with chemistry (WRF/Chem), Atmospheric Environment, 44, 3568–3582, https://doi.org/10.1016/j.atmosenv.2010.05.056, 2010.
- 515 Zhao, A., Bollasina, M. A., and Stevenson, D. S.: Strong Influence of Aerosol Reductions on Future Heatwaves, Geophysical Research Letters, 46, 4913–4923, https://doi.org/10.1029/2019GL082269, 2019.